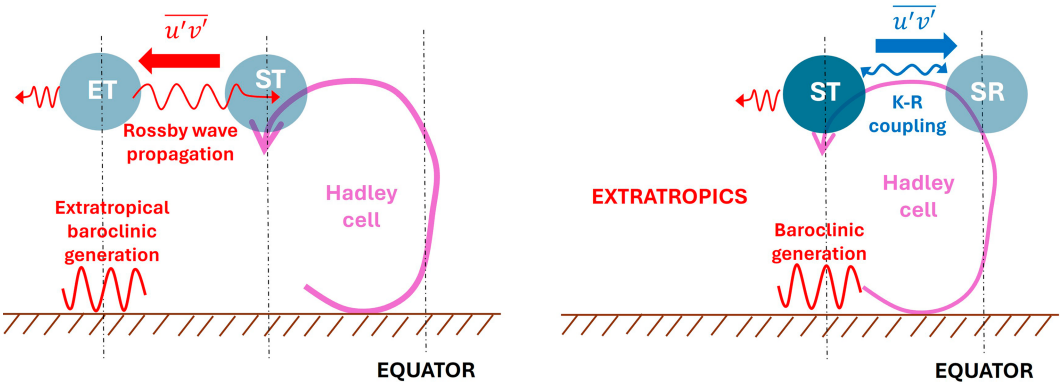

FIG. 1. Sketch illustrating the transition to superrotation when varying the latitude of the baroclinic zone in a terrestrial dry dynamical core (see Z22 for details). The balloons show wind extrema corresponding to the extratropical (ET), subtropical (ST), or superrotating (SR) jets and are shown darker for stronger jets. The red (blue) symbols and text denote extratropical (tropical) eddy processes, and the purple line shows the Hadley cell (stronger when thicker). (left) In an Earth-like climate, baroclinic eddies generated in the extratropics propagate equatorward and break in the subtropics, extracting momentum from the subtropics and forcing the extratropical jet at the expense of the subtropical jet. With a slow subtropical jet, Kelvin–Rossby instability cannot occur. (right) When baroclinic generation moves to the subtropics, baroclinic eddies no longer decelerate the subtropical jet and the ensuing large upper-tropospheric wind shear facilitates Kelvin–Rossby coupling (double arrow). Kelvin–Rossby instability then transports the subtropical jet momentum towards the equator, producing superrotation. The Hadley cell is stronger in an Earth-like climate.

have provided evidence for the relevance of Kelvin–Rossby coupling for the superrotation of Venus and Newman et al. (2011) and Lewis et al. (2023) for the stratosphere of Titan.

It seems reasonable that Kelvin–Rossby instability should emerge in small and/or slowly rotating planets. In that limit, the equatorial deformation radius has planetary scale, making it easier for the Kelvin wave to overlap with extratropical Rossby waves. From this perspective, Earth is too large and rotates too fast to support Kelvin–Rossby instability. However, we have recently shown (Zurita-Gotor et al. 2022, hereafter Z22) that it is possible to get Kelvin–Rossby instability and superrotation in a dry dynamical core with terrestrial parameters by moving the baroclinic zone equatorward, explaining previous results by Williams (2003).

While moving the baroclinic zone equatorward should increase the spatial overlap between Kelvin and Rossby waves, Z22 argued that the key factor for the transition to superrotation in their simulations was the reduction in the extratropical eddy drag when the baroclinicity moves equatorward. Z22 noted that extratropical eddies prevent superrotation in an Earth-like setting not just because they decelerate the tropical winds (e.g., Laraia and Schneider 2015) but also because they hamper Kelvin–Rossby instability. Figure 1 illustrates this argument. In an Earth-like climate (left), baroclinic eddies generated in the extratropics preferentially propagate equatorward and break in the subtropics, decelerating the subtropical jet. With a slow subtropical jet, Kelvin–Rossby instability is inhibited because the equatorial Kelvin wave moves too fast eastward to phaselock with the subtropical planetary Rossby wave. [As noted by Zurita-Gotor and Held (2018), Kelvin–Rossby instability is enhanced with increasing meridional shear and attains the maximum growth rate in the angular momentum conserving/zero vorticity limit.] In contrast, when the baroclinic eddy generation moves closer to the subtropics (Fig. 1, right), there is less meridional Rossby propagation, with more of the dissipation of the waves occurring near the region of generation and little deceleration of the subtropical jet. Of the remaining propagation, there is a preference for cyclonic wave breaking and momentum transport into the jet from higher latitudes. The ensuing large meridional shear in the tropical upper troposphere facilitates Kelvin–Rossby instability, which equilibrates by transporting momentum equatorward and driving superrotation.

This argument implies that both the extratropical eddy-driven jet and the equatorial westerlies in a superrotating flow feed from the momentum created in the subtropics by the Hadley cell. From this perspective, whether the flow superrotates or not likely depends on which process is dominant. In an Earth-like climate, the strong baroclinic eddies prevent superrotation. In contrast, as the Hadley cell extends to high latitudes in a small/slowly rotating planet, the baroclinic eddies are weak and have little room to propagate—the subtropical jet then remains strong enough to allow Kelvin–Rossby instability and superrotation.

While an equatorial eddy acceleration S_{eddy} is a prerequisite for superrotation (Hide 1969), the strength of the ensuing westerlies will ultimately be determined by the balance between terms accelerating and decelerating the equatorial winds. Specifically, we can approximate the equatorial momentum balance above the boundary layer as

$$[\overline{\omega}]\partial_p[\overline{u}] \approx S_{\text{eddy}}$$

where S_{eddy} is the equatorial eddy forcing and square brackets (overbars) indicate zonal (temporal) averages. A positive S_{eddy} in the upper troposphere produces a westerly shear and is balanced in equilibrium by the deceleration by the vertical

advection by the Hadley cell (Shell and Held 2004; Caballero and Carlson 2018). Extratropical eddies may affect this balance in different ways. They can reduce S_{eddy}, directly when they break sufficiently deep in the tropics, or indirectly by impeding Kelvin–Rossby instability as in the Z22 simulations. But they can also augment the Hadley cell drag by contributing to the driving of the Hadley cell (Walker and Schneider 2006). While the ratio of equatorward versus poleward momentum flux out of the subtropical jet is a nondimensional metric that likely helps us understand the sensitivity of superrotation, it is not obvious how to convert this ratio into an estimate for the magnitude of the equatorial zonal wind given all these different possibilities.

This study aims to evaluate the value of an idealized moist GCM as a tool to study superrotation and to examine different perspectives on how the strength of superrotation is controlled. Similar to Z22, we consider a suite of simulations in which baroclinic eddies move gradually equatorward, which is achieved by flattening the high-latitude SST gradient in an idealized aquaplanet. This will be shown to produce superrotation. In addition to the simulations in which the latitudinal SST profile is altered, we also examine simulations in which SSTs are raised or lowered uniformly, to test our understanding from this different direction.

The use of this more complex model raises a number of additional complications not present in Z22. These include the following: how does the phase speed of the convectively coupled Kelvin wave in this model affect superrotation?; to what extent can the effect of the convective parameterization on superrotation be understood from the strength of the Hadley cell?; and does the treatment of convection affect the response of superrotation to uniform warming or cooling?

To investigate these questions, we follow a similar approach to Z22 in an idealized moist GCM. Section 2 describes the specifics of the model and the procedure used for moving the eddy generation equatorward. Section 3 compares the control simulation produced by the model using two different convective closures. Section 4 maps the transition to superrotation in both model versions and describes the changes in the mean circulation in the simulations. Section 5 analyzes the role played by the eddy fluxes in the transition to superrotation and investigates the impact of Kelvin–Rossby coupling for the equatorial eddy acceleration. Section 6 describes the sensitivity of superrotation when the model warms uniformly. We conclude with a summary and a discussion in section 7.

2. Model description

We employ in this study the idealized moist GCM available in the Isca code repository (Vallis et al. 2018) maintained at the University of Exeter (https://github.com/ExeClim/Isca). The model is based on the idealized moist physics described in Frierson et al. (2006), except that full radiation is used instead of gray radiation following Jucker and Gerber (2017). The model advects water vapor but carries no liquid water—the condensate is rained immediately upon saturation and there are no clouds. In the version used in this paper, the falling rain is reevaporated and only reaches the surface when all the layers below are saturated. Radiation is modeled using the RRTMG algorithm (Mlawer et al. 1997), with the obliquity and eccentricity set to zero to eliminate the seasonal cycle but keeping the diurnal cycle. CO_2 is the only radiatively active species besides water vapor and has a constant concentration of 300 ppmv. The solar constant is 1365 W m^{-2} and the surface albedo 0.26 to generate an Earth-like planetary albedo in the absence of clouds. We use terrestrial values for the planet radius and rotation rate. To facilitate reproducibility of our results, a sample control runscript is included as in the online supplemental material.

We use two different versions of the model differing only in the convective closure. One version of the model uses the simplified Betts–Miller scheme introduced by Frierson (2007a), with the modifications introduced by O'Gorman and Schneider (2008). This scheme relaxes temperature to a moist adiabat and humidity to a constant RH of 70% with a convective time scale of 2 h. It treats nonprecipitating shallow convection as occurring when there is not enough column water for the relaxation of temperature and moisture to consistently extend to the level of neutral buoyancy with positive precipitation. The version of this shallow scheme that we utilize is referred to by Frierson (2007a) as "shallower." There is no parameterized momentum transport in this convection scheme. We will refer to this version of the model as SBM. For the parameters considered here, the bulk of the tropical precipitation in the SBM model is parameterized as opposed to being produced by condensation on the resolved scales.

Alternatively, we have also performed simulations with no convective parameterization, using large-scale condensation (LSC) only. The SBM and LSC models epitomize two limits of tropical stabilization across classes of convective closures. In the terminology of Neelin and Held (1987), they produce very different tropical gross moist stability (GMS) for the mean motion. The SBM model produces a positive GMS throughout the tropics. In contrast, the LSC model produces a negative GMS at the ITCZ and energy export out of the ITCZ is performed by the transient eddy moisture flux (Frierson 2007a; Zurita-Gotor et al. 2023). Zurita-Gotor et al. (2023) show that this negative GMS favors an instability in the location of the ITCZ and the existence of multiple equilibria when using a slab ocean boundary condition with sufficient depth. We run the model here using fixed-SST boundary conditions, which precludes this ITCZ instability.

The SST profiles that we use are based on the control profile of Neale and Hoskins (2000). In this profile (thick black line in Fig. 2), temperature decreases with a squared cosine form from an equatorial maximum of 300 to 273 K at 60°, remaining flat beyond that latitude as a simple model for ice. We consider variations of this profile in which the SST flattens at increasingly warmer temperatures T_m, which has the effect of shrinking the baroclinic zone on its poleward side and we will show to push the baroclinic eddies equatorward. Note that this manipulation of the meridional temperature gradient is different from that used by Z22, who changed the length scale over which temperature decreases from the equator to the pole while keeping the net temperature difference constant. Our motivation for using this alternative setup is the desire to

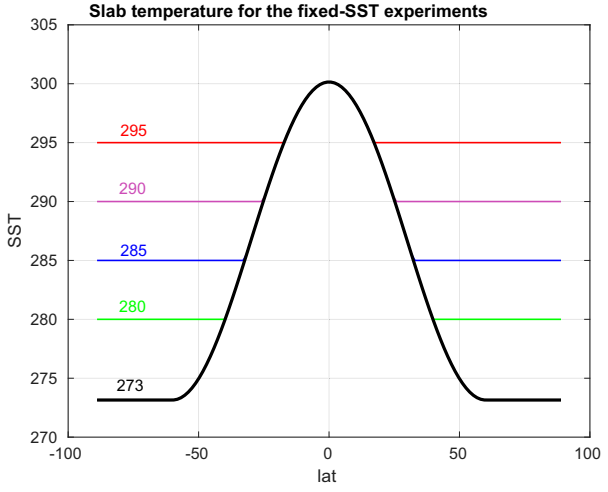

FIG. 2. SST profiles used in this study. In the standard Neale and Hoskins (2000) profile (thick black), SST decreases until reaching a minimum temperature $T_m = 273$ at 60° and flattens poleward of this latitude. We consider a suite of simulations changing the temperature T_m at which SST flattens (colored lines), which shrinks the baroclinic zone and pushes the extratropical eddies equatorward.

keep the tropical SSTs unchanged when T_m varies so that changes in T_m do not directly affect the driving of the Hadley cell when the region with flat SSTs does not intrude into the tropics.

We consider T_m values ranging from $T_m = 273$ K (the standard Neale and Hoskins setup) to $T_m = 295$ K, for which the region with flat SSTs intrudes well into the tropics. For later reference, the transition to a flat SST occurs at latitudes of 40°, 32°, 25°, and 17° for $T_m = 280$, 285, 290, and 295 K, respectively. The $T_m = 273$ K case is also referred to as the control in the following.

The simulations described in this paper were run at T85 resolution. Very small differences were found when some of these simulations were repeated at higher resolution. The model has 40 uneven sigma levels, with 15 of these levels located above $\sigma = 0.1$ and the top full level at $\sigma = 0.0012$. A sponge with viscosity $\mu = 5 \times 10^7$ m^2 s^{-1} damps the eddies at the top model level. A sensitivity analysis using stronger and/or deeper sponges was performed to ensure that the results presented in this paper are not substantially affected by spurious reflections at the model top.

3. The SBM and LSC control climates

We start by comparing the control climate produced in the standard Neale and Hoskins (2000) setup with our two choices of convective closure (Fig. 3). Our simulations agree with those of the aquaplanet intercomparison project [Aqua-Planet Experiment (APE)] using more comprehensive atmospheric models, as described in Blackburn et al. (2013), in that they produce a strong Hadley cell and a strong $O(60)$ m s^{-1} subtropical jet. (These aquaplanet Hadley cells are comparable in strength to the wintertime rather than the annual mean or equinoctial terrestrial cells.) The jet is slightly faster and equatorward in the simulation with no convective scheme, which also displays weak upper-tropospheric superrotation. In contrast, the SBM simulation produces easterlies in the upper troposphere (Fig. 3d). Both models produce superrotation in the stratosphere. The fields shown are averaged over 2000 days after the model has spun up.

The two simulations differ markedly in the tropics. While the LSC simulation produces a sharp equatorial precipitation maximum, the SBM climate features a broad precipitation maximum with a hint of a double ITCZ. The latter is a common occurrence across many of the APE models (Blackburn et al. 2013). Consistent with these precipitation differences, the Hadley circulation is also very different in the two models. The LSC Hadley cell is stronger, but the two circulations differ especially in their spatial structure (cf. the top two panels of Fig. 3). Besides having a narrower and stronger updraft, the LSC circulation reaches its maximum in the lower troposphere. In contrast, the weaker SBM circulation peaks at upper levels and is more disconnected from the surface. While the maximum in the Hadley streamfunction is somewhat larger in LSC than in SBM [315 Sv (1 Sv $\equiv 10^6$ m^3 s^{-1}) compared to 255 Sv], due to this difference in vertical structure, the equatorward mass transport below 800 hPa is 50% larger in LSC than in SBM. In addition, the wider ITCZ in SBM upwells lower-angular-momentum air into the upper troposphere as compared to the more equatorially confined ITCZ in LSC, consistent with the upper-level equatorial easterlies in SBM.

Frierson (2007b) describes an aquaplanet model with the SBM convective closure which supports a well-defined convectively coupled Kelvin wave with a phase speed of 18 m s^{-1}. We also find a Kelvin wave in our SBM control, but with a faster phase speed of 27–28 m s^{-1}. In addition, we find a somewhat less distinct Kelvin wave in our LSC control with essentially the same phase speed, while Frierson (2007b) does not find a well-defined Kelvin wave in their LSC configuration. The largest differences between the two models are the inclusion in the present model of realistic clear-sky radiation rather than a gray model and the use here of fixed SST boundary conditions rather than a slab ocean, but we do not understand how these translate into a faster Kelvin wave. The implication is that the Kelvin wave in our model is in some sense less strongly coupled to moist convection although it still is accompanied by a precipitation signal. Some properties of the Kelvin wave in the SBM and LSC models are described in section 6.

4. Sensitivity to T_m

Both the SBM and LSC models produce the strongest superrotation around $T_m = 290$ K (Fig. 4, top), when the poleward region with flat SSTs extends to the Hadley cell edge. The equatorial westerlies decrease slightly as T_m increases further. The zonal wind in the two models also exhibits a qualitatively similar sensitivity to T_m. In both models, the jet moves equatorward (Fig. 4, middle), and the equatorial westerlies both strengthen and expand downward (Fig. 4, bottom) when

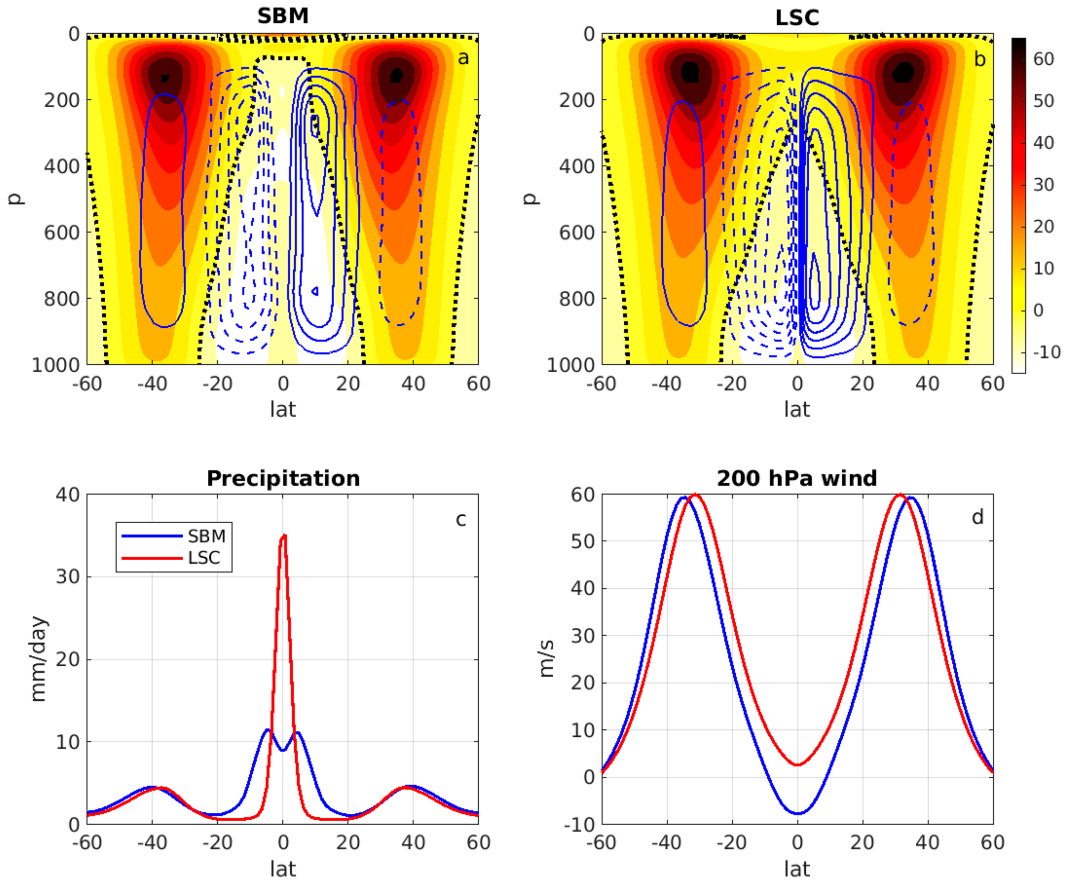

FIG. 3. (top) Zonal-mean zonal wind (shading, the black dotted line marks the zero contour) and mean meridional circulation (blue contours, contour interval 50 Sv) for the control APE simulations with the (left) SBM and (right) LSC models. (bottom left) Mean precipitation for the same two simulations. (bottom right) Zonal wind at 200 hPa for the same simulations.

T_m increases. However, the strength of the superrotation is very different in the two models: while the equatorial westerlies increase only slightly relative to control in LSC, strong westerlies exceeding 30 m s^{-1} are found for SBM.

The zonal wind sensitivity in our SBM simulations is reminiscent of that found by Z22 in their dry model when the baroclinicity is moved equatorward. But in contrast to that model, the transition to strong superrotation occurs gradually rather than abruptly. We have looked at other intermediate cases beyond those shown in Fig. 4 to confirm this continuity and the absence of hysteresis. We believe this difference may be due to the weaker diabatic forcing in the Z22 model, which uses a long forcing time scale of 40 days both in the interior and near the surface. This choice of weak radiative restoring was made to maintain close contact with the results of Williams (2003) that motivated the Z22 study. We have more recently found that strengthening the restoring of temperatures near the surface, following the specification in Held and Suarez (1994), results in a smoother transition without hysteresis in that dry model. If the prescribed SSTs in the present moist model were replaced with a slab ocean boundary condition, the restoring at the surface of the time-averaged temperatures would be weaker and could result in an abrupt transition. Preliminary simulations of this type have introduced additional issues that will need to be addressed elsewhere. The detailed explanation for why this strength of the temperature restoration affects abruptness of the transition also requires further study.

The equatorial westerlies in our SBM simulations are the most variable at the intermediate value T_m = 285-K around which an abrupt transition might have been expected based on the dry model results in Z22. The standard deviation of the daily zonal mean equatorial wind at 200 hPa is 2.3, 3.3, 5.2, 2.6, and 2.8 m s^{-1} for the simulations with T_m = 273, 280, 285, 290, and 295 K, respectively. We will focus on the 285-K simulation with the strongest variability in the diagnostics presented in the next section.

The Hadley cell upwelling brings in low-angular-momentum air and damps the upper-troposphere equatorial westerlies. Therefore, the differences in the Hadley cell (Fig. 3) may partly explain the different superrotation of the two models (Pinto and Mitchell 2014). Figure 5 (top) shows that the equatorial upwelling is roughly twice as large in the LSC model as in the SBM model in the APE setting. The different strength

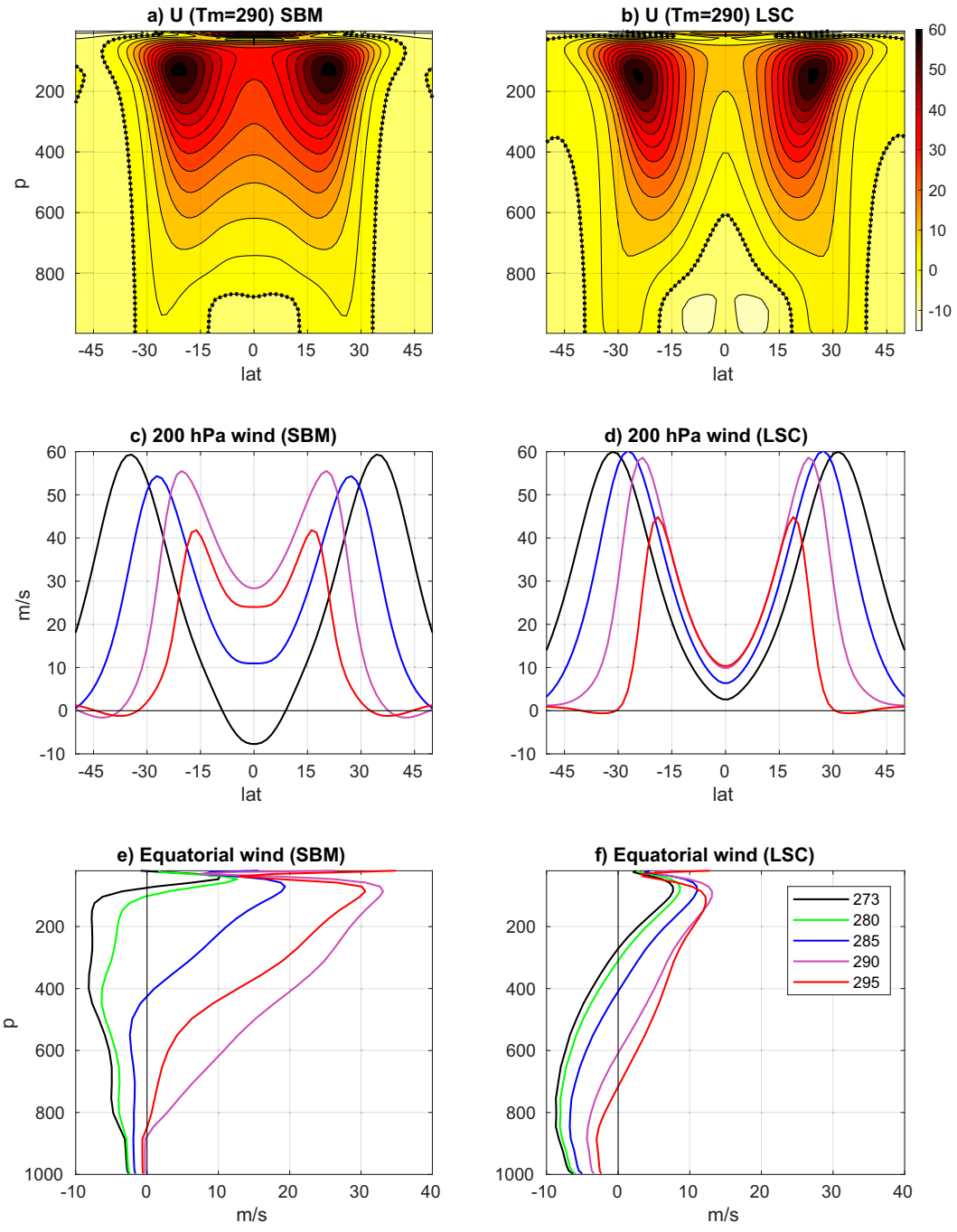

FIG. 4. For the (left) SBM and (right) LSC models: (top) Mean zonal wind for $T_m = 290$ K with contour interval of 5 m s^{-1} and with a dotted black line marking the zero contour. (middle) Mean zonal wind at 200 hPa as a function of T_m. (bottom) Mean zonal wind at the equator as a function of T_m. Note that the $T_m = 280$ K has been omitted from the middle panels for clarity.

of upwelling in the two models is, in turn, likely due to the larger gross moist stability as mentioned in section 2.

As T_m increases, the Hadley cell weakens in both models as expected from the reduced subtropical eddy cooling associated with a reduction in the poleward eddy energy flux as well as from reduced upper-tropospheric eddy momentum fluxes. (The response of these eddy fluxes to T_m will be described in the next section.) However, the equatorial upwelling decreases much more for the SBM model than for the LSC model, especially at lower levels. For $T_m = 290$ K, the Hadley circulation of the SBM model is nearly disconnected from the surface (Fig. 5, bottom), shielding the upper-tropospheric

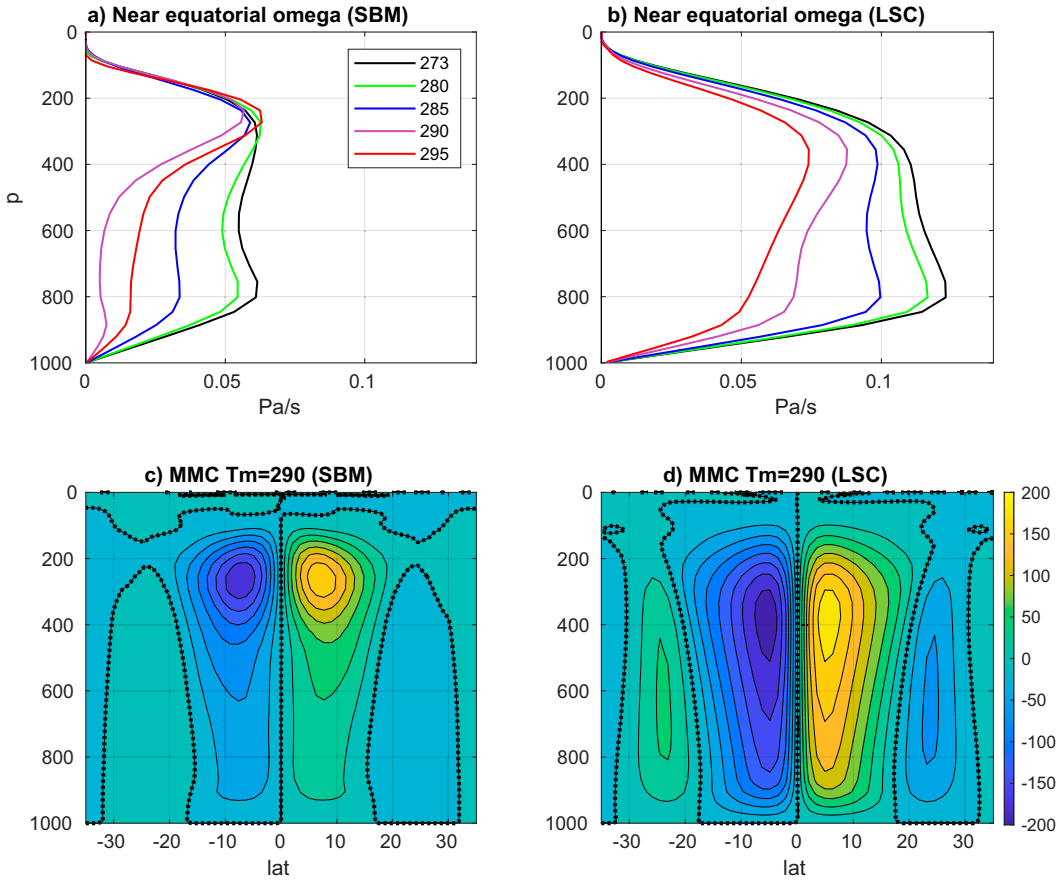

FIG. 5. For the (left) SBM and (right) LSC models: (top) Near-equatorial (5°S–5°N average) upward pressure velocity for different T_m values. (bottom) Mean meridional circulation (contour interval 25 Sv) for $T_m = 290$ K, which gives the maximum superrotation in both models.

equatorial westerlies from surface friction. This lifting of the Hadley cell off the surface is consistent with the behavior of axisymmetric Hadley cell models in the absence of extratropical eddy fluxes (Fang and Tung 1996; Singh and Kuang 2016). The more drastic weakening of the vertical velocity in SBM than in LSC is consistent with a greater superrotation in that model, given the greater weakening of the drag due to the upwelling in the Hadley cell.

5. Waves driving and impeding superrotation

We next investigate the role played by tropical and extratropical eddies in the transition to superrotation in our simulations. The former drive superrotation, while the latter impede it.

As discussed in introduction, both the extratropical jet in an Earth-like climate and the equatorial westerlies in a superrotating climate feed from the momentum deposited in the subtropics by the Hadley cell. This suggests that the partition of the subtropical eddy momentum divergence into extratropical and tropical convergence may be a useful indicator for delineating the transition to superrotation. We compute this partition using the procedure illustrated in Fig. 6 (top) for the $T_m = 285$ K simulation. All eddy momentum fluxes are vertically averaged above 500 hPa.

We first locate the latitude ϕ_M of maximum eddy momentum divergence and the nearest latitudes of zero momentum divergence poleward and equatorward of this maximum for each simulation, ϕ_P and ϕ_E. The net subtropical divergence is then defined as the integrated eddy momentum divergence between these two zeros (black area), and the net extratropical/tropical convergence as the outward eddy momentum flux across the latitudes ϕ_P and ϕ_E. These correspond to the blue and red areas, respectively. Note that by including poleward regions of eddy momentum divergence that compensate part of the extratropical convergence, the blue area is an indicator of the eddy momentum convergence effectively associated with tropical–extratropical momentum exchange. Because the eddy momentum flux vanishes at the pole, this area must also equal the eddy momentum flux across the latitude ϕ_P.

The middle and bottom panels of Fig. 6 describe the sensitivity of these areas to T_m for the two models. For SBM (Fig. 6, middle), the tropical convergence is negligible in the control APE setting and starts increasing as the jet moves equatorward (cf. Fig. 4). It reaches its maximum value when the jet

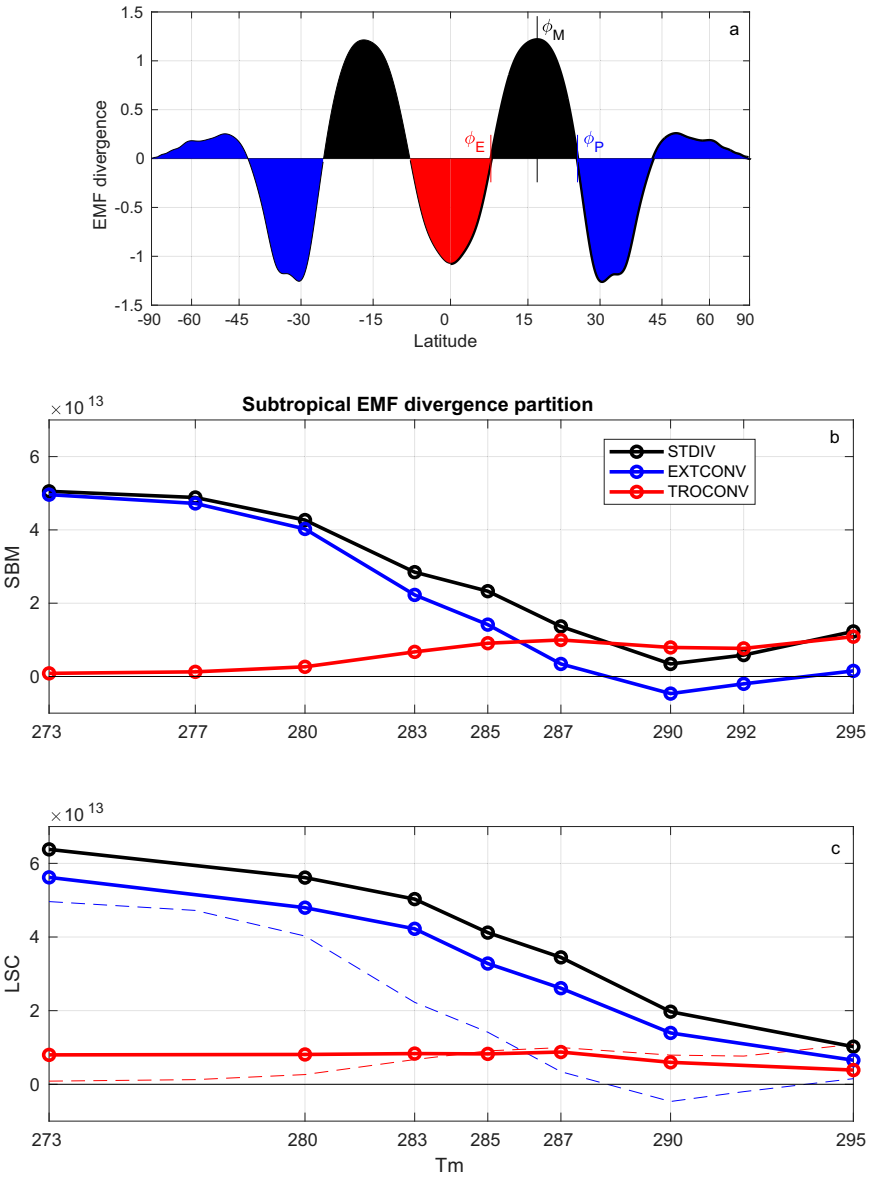

FIG. 6. (top) Latitudinal distribution of the eddy momentum flux divergence (vertically integrated above 500 hPa) for the T_m = 285 K simulation. The net subtropical divergence is computed as the black area in the this figure, and the net extratropical (tropical) convergence as the blue (red) areas. See text for details. (middle) Sensitivity to T_m of the net subtropical eddy momentum divergence (black), extratropical eddy momentum convergence (blue), and tropical eddy momentum convergence (red) in the SBM model. (bottom) As in (middle), but for the LSC model, with the SBM results shown with a thin dashed line for comparison. In both panels, the vertical grid lines emphasize the specific simulations performed.

approaches the subtropics ($T_m \approx 287$ K) and changes little beyond that point. This maximum tropical convergence is nevertheless much weaker than the extratropical convergence in the control, suggesting that the strong decrease in the extratropical drag when T_m increases is important for superrotation. As a result of this decrease, the tropical convergence exceeds the extratropical convergence for T_m values above 285 K, coinciding with the regime of strong superrotation.

The corresponding results for the LSC model are shown in the bottom panel of Fig. 6. In this model, the tropical eddy momentum convergence is already present in the control T_m setting (consistent with the weak superrotation in that simulation). The tropical momentum convergence changes little with T_m, suggesting that the enhanced superrotation when T_m increases is due to the reduction in the extratropical drag. But because this drag does not decrease as strongly as in the SBM

model, the tropical convergence never becomes dominant in the LSC model.

Overall, Fig. 6 suggests that while Kelvin–Rossby instability (or some other form of eddy acceleration) is required for superrotation, the enhanced superrotation when T_m increases in our runs is not primarily due to increased destabilization of the tropical winds. In contrast to the schematic in Fig. 1 and the previous Z22 results, the subtropical jet speed is only weakly enhanced by the reduction in extratropical drag in these simulations. We argue in section 7 that the effect of extratropical drag on superrotation is not direct, but is rather mediated in large part by the induced weakening of the Hadley cell and the associated reduction in drag due to equatorial upwelling.

a. *Tropical eddy driving and evidence of Kelvin–Rossby coupling*

As shown above, there is significant equatorial eddy momentum convergence at the equator for all values of T_m in the LSC model and for $T_m \gtrsim 283$ K in the SBM model. We next analyze the structure and generation of the waves producing this acceleration. We will focus on the SBM simulation with $T_m = 285$ K, which marks the transition to strong superrotation in that model and displays the strongest equatorial zonal wind variability in the equilibrated state for all values of T_m considered. To analyze the waves responsible for the model's spinup, we examine an ensemble of 40 different 200-day simulations initialized from rest with random small noise. Figure 7a provides an overview of the variability of the upper-tropospheric equatorial zonal wind in this ensemble, whereas Fig. 7b shows the ensemble-mean evolution of the equatorial wind.

The equatorial acceleration driving superrotation at upper-tropospheric levels is imparted by meridional eddy angular momentum convergence, with the vertical eddy momentum flux spreading this forcing vertically (not shown). We can decompose the meridional eddy convergence as the sum of the eddy vorticity flux and the divergent eddy acceleration:

$$-\frac{1}{a\cos^2\phi}\frac{\partial}{\partial\phi}(\overline{u'v'}\cos^2\phi) = \overline{v'\xi'} - \overline{u'D'}. \qquad (1)$$

As noted by Zurita-Gotor (2019) in an observational study, while the eddy vorticity flux dominates in the terrestrial extratropics, where it forces the eddy-driven jet, the divergent term $-\overline{u'D'}$ is more important for equatorial eddy acceleration. Z22 found that this term was responsible for driving superrotation in their dry simulations. Figure 7c shows that the same is true in this idealized model, with the ensemble-mean acceleration reaching values as large as 8 m s^{-1} day^{-1} during the spinup. In contrast, the eddy vorticity flux is much weaker and mostly negative at the equator (not shown), which suggests that the generation of Rossby waves by convective vorticity forcing (Suhas et al. 2017) is not driving superrotation in these simulations.

To identify the eddies imparting this acceleration, Fig. 7d (blue line) shows the zonal $-\overline{u'D'}$ cospectrum and Fig. 7e its space-time cospectrum, both at 200 hPa. The equatorial acceleration is strongly dominated by a fast $k = 1$ Kelvin wave with a phase speed of about 28 m s^{-1}. Figure 7e indicates that there is a spectrum of Kelvin waves with the same phase speed, with $k = 1$ producing the strongest contribution to the equatorial acceleration. The precipitation spectrum is dominated by the same modes (not shown).

A similar peak in $-\overline{u'D'}$ associated with a planetary equatorial Kelvin wave was found in the dry simulations of Z22. It was argued in that work that the Kelvin wave and the equatorial acceleration were generated by Kelvin–Rossby instability, as there is no other obvious source of a Kelvin wave in that model (the radiative equilibrium profile used was convectively stable.) In the present moist simulations, with radiation destabilizing the atmosphere to convection, however, the Kelvin wave has an independent existence as a convectively coupled wave regardless of whether it couples with the subtropical Rossby wave or not.

The integral over latitude of $-\overline{u'D'}$ must be balanced by the integral over latitude of $\overline{v'\xi'}$ level by level since they sum to the divergence of the angular eddy momentum flux. Figure 8 (top) shows that the divergent $k = 1$ acceleration centered on the equator is balanced by the deceleration associated with a negative eddy vorticity flux between 10° and 20° latitude. This is consistent with the forcing of a subtropical Rossby wave by the equatorial Kelvin wave, but there is also evidence that the interaction goes both ways and the subtropical Rossby wave contributes to forcing the Kelvin wave. To show this, we first note that the Kelvin pseudomomentum forcing $-\overline{u'D'}$ is dominated by $-\overline{u'_rD'}$ (cf. black and red lines in Fig. 8c), where $u'_r = -\partial_y\psi'$ is the rotational zonal velocity and the streamfunction ψ' is related to the vorticity ξ' through the relation $\nabla^2\psi' = \xi'$. Piecewise vorticity inversion (Davis 1992) then allows us to estimate the contributions to $-\overline{u'_rD'}$ computed using the streamfunction calculated from the inversion of the vorticity anomalies in different regions. Figure 8c shows that roughly half of the forcing is associated with zonal wind anomalies induced by vorticity anomalies outside the deep tropics ($|\phi| > 10$, dashed red line).

Although pure modal growth of Kelvin–Rossby modes is not expected given the variability from other sources present in this model, the composite growth during the spinup is nevertheless nearly exponential and the composite $k = 1$ anomaly is consistent with the expected structure and growth mechanism for these modes. Figure 8d shows the composite anomaly at $t = 36$ days, near the end of the spinup period (black vertical line in Fig. 8c). To avoid cancellation, all fields have been longitudinally shifted before averaging so that the geopotential has the same phase at the equator in all ensemble members (the same shift is applied at all latitudes and to other fields). The composite anomaly has a mixed Kelvin–Rossby structure, although with weak subtropical amplitude. In particular, the eddy geopotential (shading) has the characteristic meridional tilt identified by previous studies of Kelvin–Rossby instability (Iga and Matsuda 2005; Wang and Mitchell 2014; Zurita-Gotor and Held 2018). This phase tilt is such that the Rossby gyres forced by the off-equatorial vorticity anomalies (vectors) produce easterly (westerly) equatorial zonal wind anomalies over longitudes of upper-level mass divergence (convergence), which gives rise to a positive zonal mean acceleration $-\overline{u'D'}$.

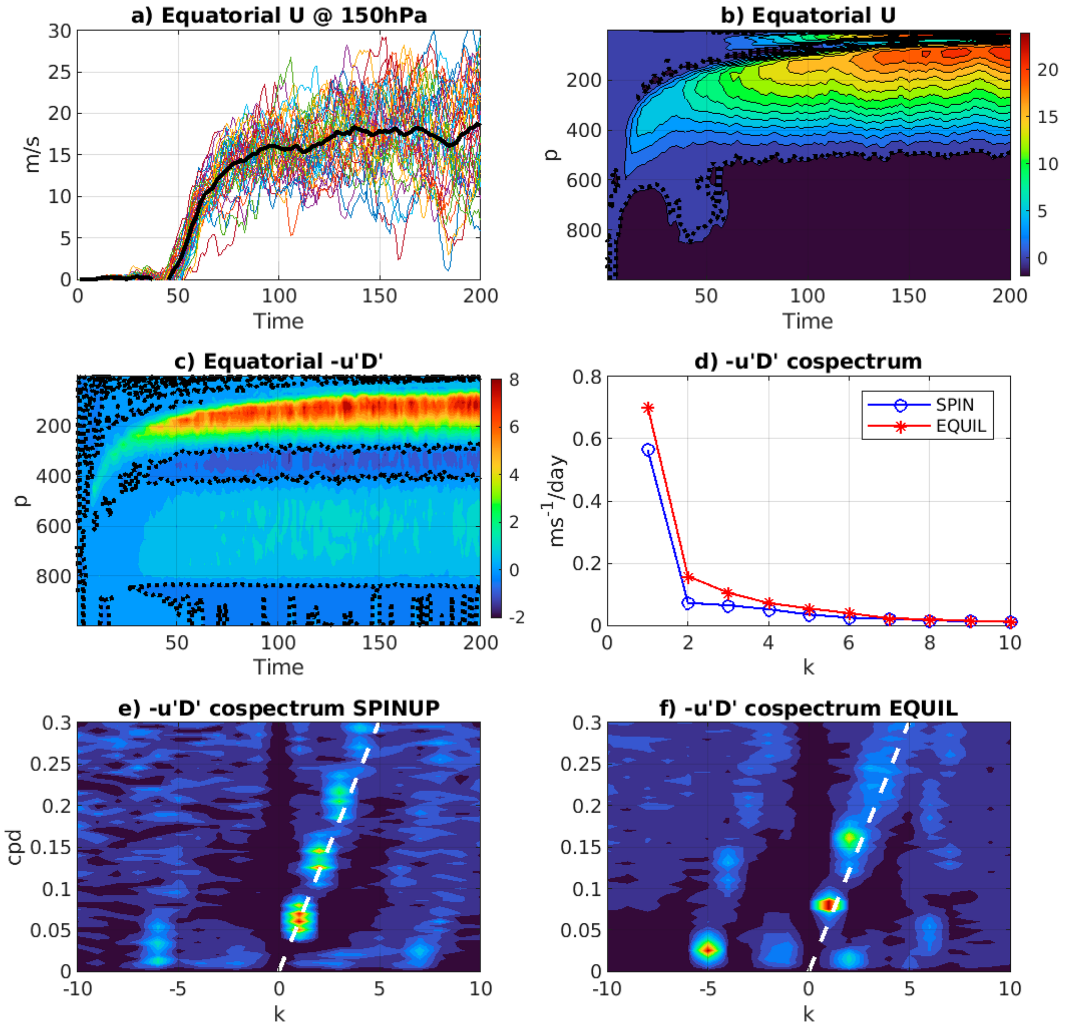

FIG. 7. For an ensemble of 40 spinup simulations with $T_m = 285$ K and using the SBM convective scheme: (a) Time series of 150-hPa equatorial zonal wind for all members (thin colored lines) and ensemble mean (thick black). (b) Time series of ensemble-mean zonal wind (m s^{-1}) at the equator. (c) Time series of the ensemble-mean divergent eddy acceleration $-\overline{u'D'}$ (m s^{-1} day^{-1}) at the equator. (d) Zonal cospectrum of the equatorial $-\overline{u'D'}$ at 200 hPa during the ensemble spinup (blue) and for the equilibrated state of a long simulation (red). (e) Space-time cospectrum of $-\overline{u'D'}$ at 200 hPa, computed over days 20–70 of the spinup simulations, and averaged within 10° of the equator. The white dashed line shows the slope corresponding to a phase speed of 28 m s^{-1}. (f) As in (e), but for the 150-hPa $-\overline{u'D'}$ at the equator during the equilibrated state of a long simulation.

We next examine the maintenance of the equatorial zonal wind in an equilibrated long simulation with $T_m = 285$ K. In the ensuing statistical equilibrium, the time-mean superrotation is maintained against the Hadley cell drag by episodes of enhanced meridional eddy momentum convergence. This eddy acceleration is again dominated by the divergent term $-\overline{u'D'}$, with a very similar zonal cospectrum to that found during the spinup (red line in Fig. 7d). The space–time cospectrum is also similar (Fig. 7f), though the Kelvin waves are faster than before ($c \approx 37$ m s^{-1}), due at least in part to the Doppler shift by the superrotating winds.

To analyze in more detail the wave-mean flow interaction during the equilibrated internal variability, we perform composites based on the value of the $k = 1$ eddy acceleration $-\overline{u'D'}$ at 150 hPa at the equator. Eighty six events separated by at least 40 days are selected for compositing, with the condition that the anomalous $-\overline{u'D'}$ exceeds 1.5σ, or roughly 9 m s^{-1} day^{-1} at the peak. Figure 9a shows the lagged composite of this index in red, with its mean value over the full time series indicated by a horizontal line. Although the peak eddy acceleration is short-lived, the eddy acceleration is significantly enhanced starting as early as 1 week before the peak.

Figure 9b shows the lagged evolution of the composite zonal wind anomaly at 200 hPa. Consistent with the previous plot, a significant westerly anomaly is seen at the equator starting around lag −5, with the maximum anomaly occurring shortly after lag zero. The westerly acceleration is preceded

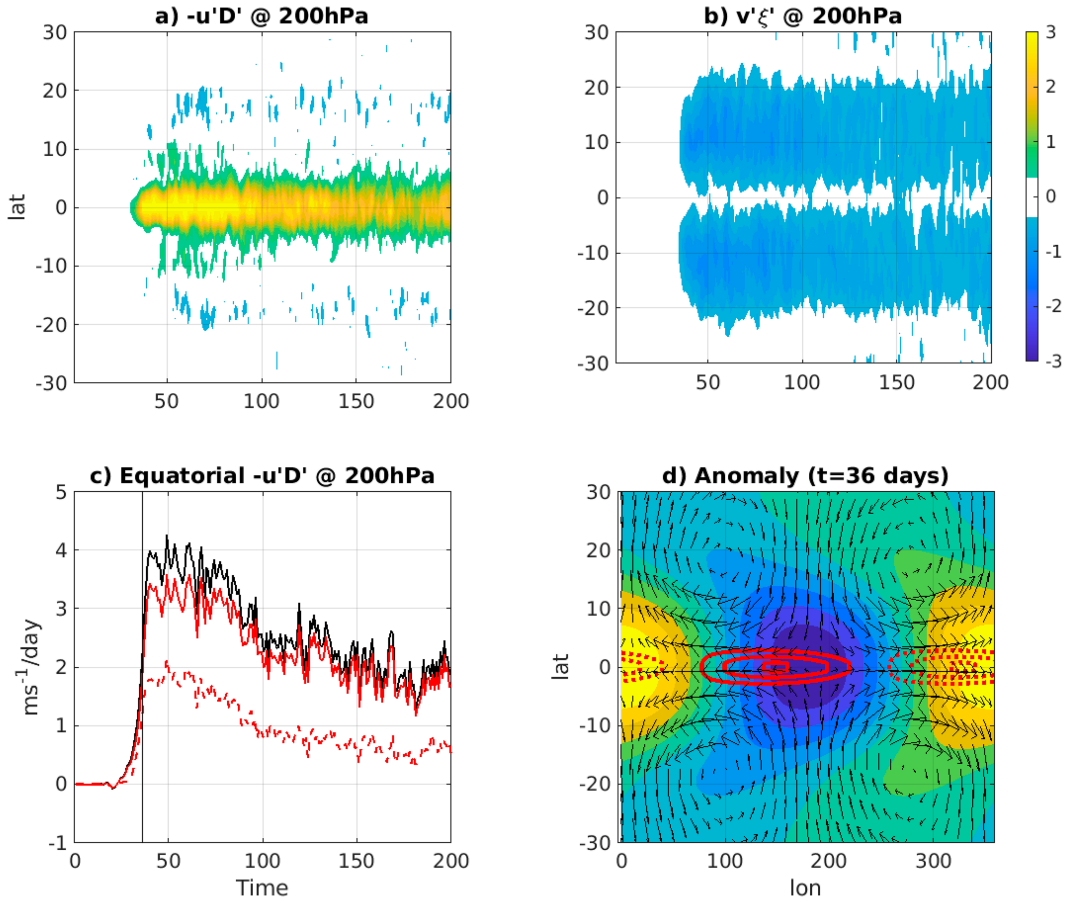

FIG. 8. (a) 200-hPa time series of the $k = 1$ divergent eddy acceleration $-\overline{u'D'}$ (m s^{-1} day^{-1}) during the ensemble-mean spinup. (b) As in (a), but for the eddy vorticity flux. (c) Time series of the ensemble-mean 200-hPa equatorial $-\overline{u'D'}$ (black) and $-\overline{u'_rD'}$ (red). The dashed red line shows $-\overline{u'_rD'}$ with u'_r computed inverting vorticity anomalies outside the deep tropics ($|\phi| > 10$) alone. (d) Composite horizontal structure of the $k = 1$ anomaly at 200 hPa on day 36 of the ensemble spinup. The shading show the geopotential, the red contours the divergence, and the vectors the rotational wind induced by vorticity anomalies outside the deep tropics.

by an extended period with easterly wind anomalies at the equator and, to a lesser extent, westerly wind anomalies in the subtropics. Both are associated with enhanced meridional shear at upper levels, which is expected to favor the Kelvin–Rossby coupling by slowing the Kelvin wave and accelerating the eastward propagation of the Rossby wave (Z22).

The anomalous eddy forcing is balanced by an enhanced Hadley cell drag $-\delta\{[\omega]\partial_p[u]\}$, where $\delta\{\cdot\}$ indicates a time anomaly. The composite evolution of the anomalous Hadley drag (averaged over the 150–350-hPa layer) is shown in Fig. 9c, together with its decomposition into contributions due to the anomalous vertical velocity and the anomalous vertical shear:

$$-\delta\{[\omega]\partial_p[u]\} \approx -[\overline{\omega}]\delta\{\partial_p[u]\} - \partial_p[\overline{u}]\delta\{[\omega]\},$$

a linearization that captures very well the full anomalous forcing (overlines indicate climatological values). The Hadley cell drag is enhanced through the eddy acceleration life cycle. The enhanced drag is initially associated with a strengthening of the Hadley cell (anomalous $[\omega]$, red) that precedes the eddy acceleration and contributes to the equatorial deceleration/subtropical acceleration noted above. The Hadley drag intensifies further due to the enhanced shear $|\partial_p[u]|$ when the equatorial westerlies spin up (blue). For larger positive lags, the Hadley cell weakens, but the Hadley cell drag remains anomalously strong due to the anomalous westerly shear.

Finally, Fig. 9d shows the composite anomaly (at lag zero) of the $k = 1$ eddies driving the acceleration. All fields have been longitudinally shifted prior to averaging as before. The structure is in good agreement with Kelvin–Rossby modes and consistent with lateral forcing of the Kelvin wave. It is interesting that the subtropical Rossby amplitude appears larger in this composite than during the spinup. A possible explanation for this difference is that the modes are primarily forced by tropical convective forcing during the spinup, with the forcing by the extratropical internal variability becoming more important during the equilibrated state. However, we have not investigated this carefully.

As during the spinup, the Rossby gyres induced by vorticity anomalies outside the deep tropics produce zonal wind anomalies that are negatively correlated with the divergence at the equator,

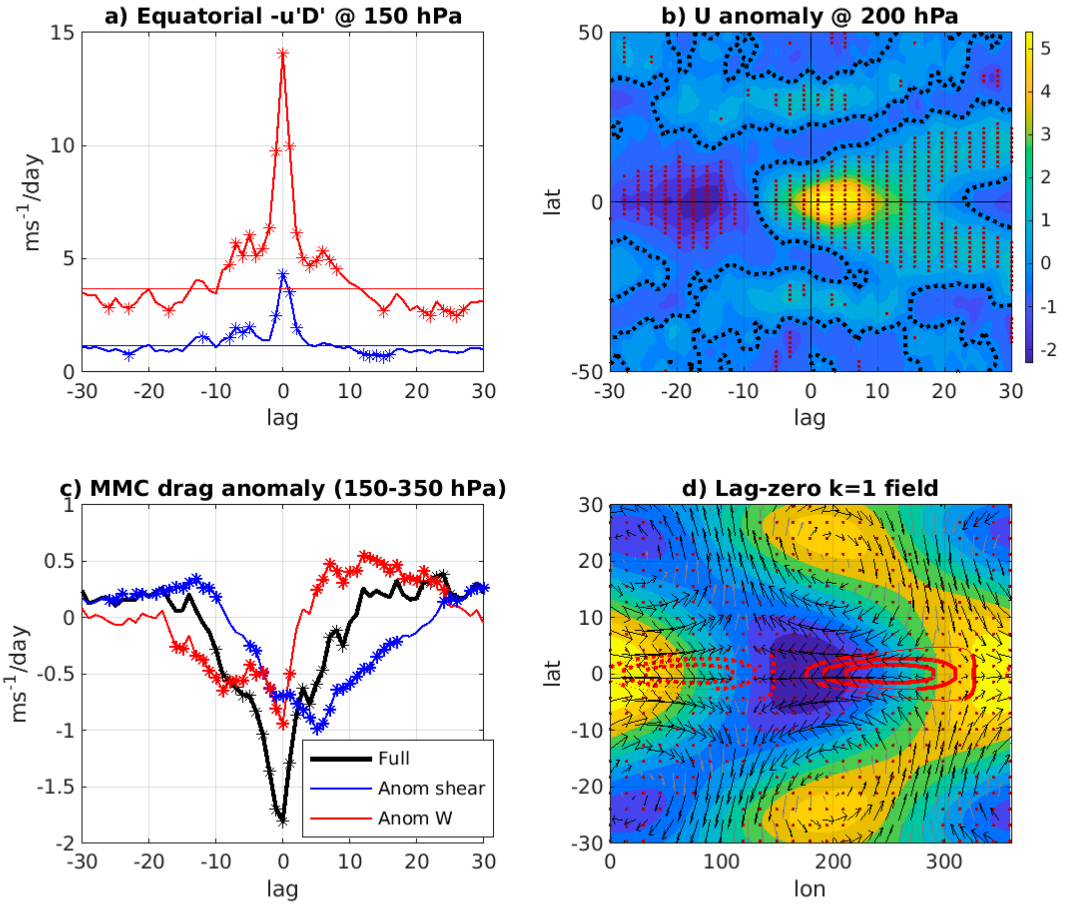

FIG. 9. For a long simulation with $T_m = 285$ K and using the SBM convective scheme: (a) Composite evolution of the equatorial $-\overline{u'D'}$ at 150 hPa (red) during acceleration events and contribution to $-\overline{u'_rD'}$ by vorticity anomalies outside the deep tropics (blue). Mean values are indicated with horizontal lines. (b) Composite evolution of the anomalous zonal-mean zonal wind at 200 hPa. (c) Composite evolution of the anomalous 150–350-hPa mean Hadley cell drag at the equator (thick black) and contributions due to the anomalous vertical velocity (red) and the anomalous vertical shear (blue). (d) Composite $k = 1$ eddy field at 150 hPa at the time of maximum acceleration. The shading shows the geopotential, the red contours show the divergence, and the vectors show the rotational wind induced by vorticity anomalies outside the deep tropics. In all panels, significance at the 95% level based on a Monte Carlo test with 500 samples is indicated with asterisks for line plots, with red stippling for shaded fields, and with thick line for contoured fields. In (d), vectors are plotted in black when the zonal velocity is statistically significant and in gray otherwise.

creating or reinforcing the Kelvin wave $-\overline{u'_rD'} > 0$. This contribution is shown with blue line in Fig. 9a. Overall, the statistically steady superrotating state is maintained by episodes of a growing Kelvin–Rossby mode similar to the growing mode that is present during the initial spinup of the superrotation. This composite picture of variability within the statistically steady sate is qualitatively similar for other values of T_m and for the LSC simulations (not shown).

b. *Sensitivity of the extratropical eddy drag*

As shown in Fig. 6, the transition to superrotation when T_m increases is accompanied in both models by a weakening of the extratropical eddy drag. However, the drag reduction is significantly more pronounced for the SBM model, which, together with the Hadley cell differences noted in section 4, helps explain the stronger superrotation in this model. To begin to address the question of why extratropical eddy momentum fluxes are so different in the two models for the same SST, we compare the changes in lower-troposphere (1000–500 hPa) baroclinic eddy generation (proportional to the eddy heat flux) and in upper-troposphere (150–350 hPa) meridional propagation (proportional to the eddy momentum flux) for the two models.

The leftmost two panels of Fig. 10 show, for the SBM and LSC models, how the lower-troposphere eddy heat flux (contours) and upper-troposphere rotational eddy vorticity flux (shading) change with T_m. The latter equals the eddy momentum convergence by the rotational motion. We focus on the rotational momentum fluxes in this figure because this helps

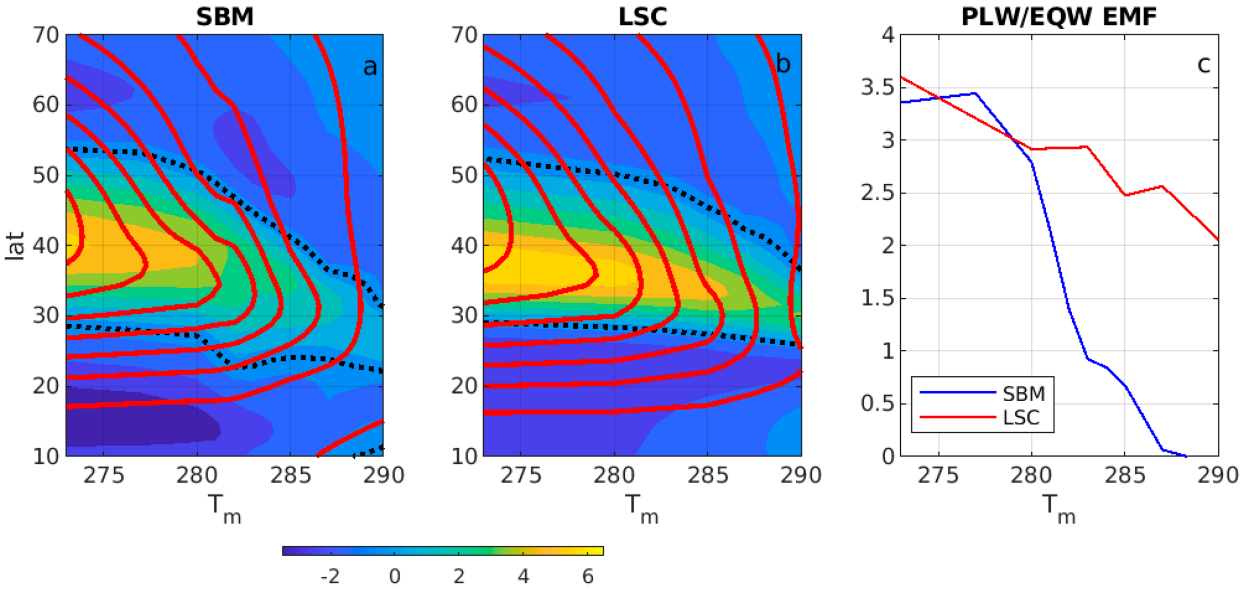

FIG. 10. (left) Vertically averaged lower-troposphere (1000–500 hPa) eddy heat flux (red contours, contour interval: 5 mK s^{-1}) and upper-troposphere (150–350 hPa) rotational eddy vorticity flux (shading, m s^{-1} day^{-1}) for the SBM model, as a function of T_m and latitude. (middle) As in the left panel, but for the LSC model. (right) Ratio between the maximum poleward and equatorward rotational eddy momentum flux for the SBM and LSC models, as a function of T_m.

isolate the extratropical forcing (Zurita-Gotor 2019), minimizing confounding effects due to changes in the tropical eddies.

As expected from the forced equatorward contraction of the baroclinic zone (Fig. 4), the lower-troposphere eddy heat flux weakens and moves equatorward as T_m increases in both models. The eddy heat flux weakens a bit more in SBM, especially at high latitudes, but differences are small. In contrast, the extratropical eddy momentum flux convergence weakens significantly more in SBM than in LSC, consistent with Fig. 6. To provide additional perspective on why the eddy momentum convergence reduces more rapidly for the SBM model, it is useful to look at how the ratio between the maximum poleward and equatorward rotational eddy momentum fluxes changes with T_m (Fig. 10c). In Earth-like climates with small T_m, the poleward eddy momentum fluxes are 3–4 times larger than the equatorward eddy momentum fluxes, indicating that eddies generated in the midlatitudes preferentially propagate equatorward. This propagation asymmetry, due to sphericity (Balasubramanian and Garner 1997), is reduced in both models when the eddy generation moves equatorward. However, the reduction is more dramatic for the SBM model for $T_m \gtrsim 282$ K, as equatorward wave propagation is strongly inhibited and eventually disappears for large T_m.

To analyze why equatorward propagation is reduced so drastically with increasing T_m for the SBM model alone, Fig. 11 shows eddy momentum flux latitude-phase speed cospectra for both models and select T_m values. Distinct signals are observed for the extratropical baroclinic waves and the tropical Kelvin–Rossby modes, which reside on different regions of the angular phase speed spectrum. Focusing on the extratropical eddies, the two models look similar in an Earth-like climate (T_m = 280 K): equatorward propagation is supported for a range of phase speeds extending from weakly westward to about 20 m s^{-1} eastward. Shorter, faster waves cannot produce a significant eddy momentum flux because they are trapped by turning latitudes on the sides of the jet. The waveguide effect increases as the jet sharpens and moves equatorward, consistent with the findings of Lee and Kim (2003) that there is little equatorward propagation when baroclinic growth occurs at the latitude of the subtropical jet. We can see in particular that as T_m increases, the maximum phase speed supporting equatorward propagation is reduced.

Only long, slow waves are able to propagate equatorward when the baroclinic generation moves to the subtropics. But as superrotation ensues for SBM, these slow waves no longer find a critical layer on the equatorward side of the jet and can now propagate through the tropics without breaking (Fig. 11c). As a result, the subtropical drag by baroclinic eddies is eliminated for both fast and slow waves (Fig. 6), which provides a positive feedback to superrotation as noted by Saravanan (1993). The extratropical drag does not weaken as much in the LSC model because superrotation is not strong enough in this model to eliminate the breaking of long baroclinic waves.

These arguments suggest that by limiting the strength of the upper-troposphere equatorial westerlies and ensuing critical layer feedback, the Hadley cell drag plays an important role for preventing in the LSC model the strong superrotation found for the SBM model. We elaborate on this view in the conclusions.

6. Sensitivity to uniform warming and cooling

To investigate the sensitivity of superrotation to the mean temperature in this model, we have also conducted experiments

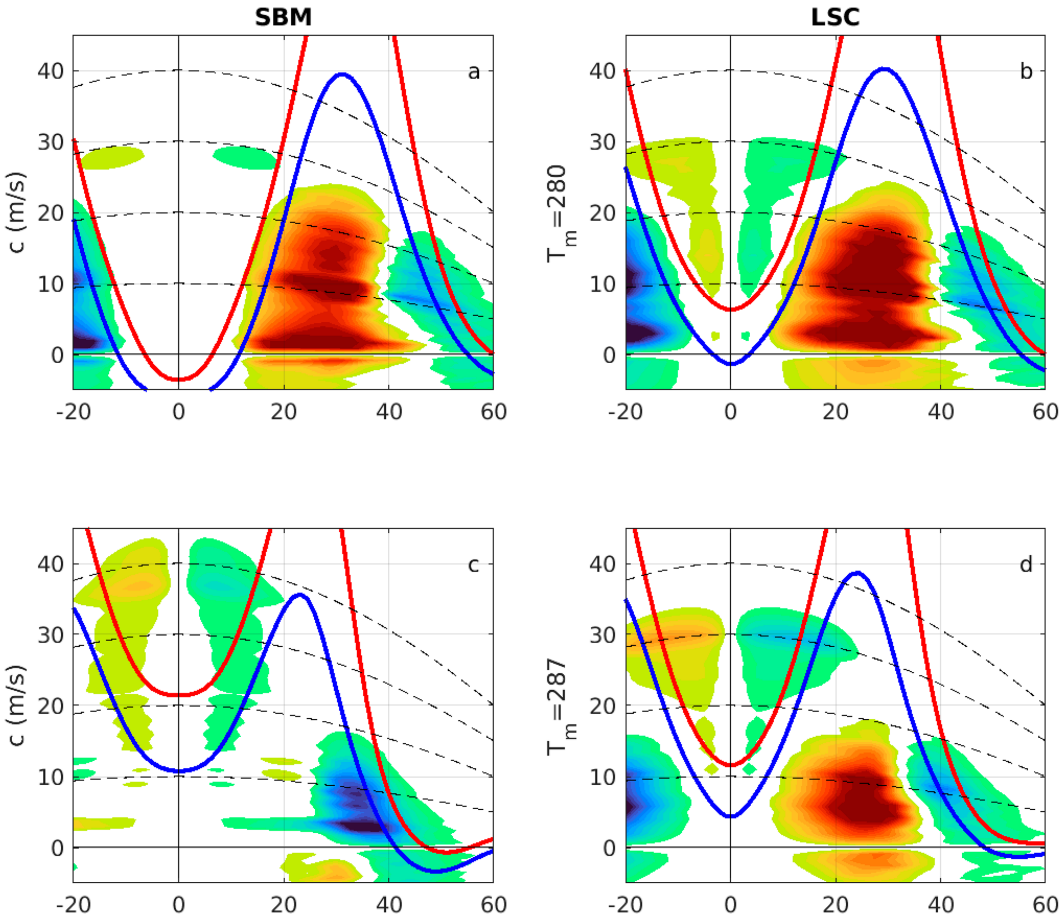

FIG. 11. For the (left) SBM and (right) LSC models and for the T_m values indicated in each row, latitude–phase speed cospectra of the upper-troposphere (150–350 hPa average) eddy momentum flux (shading) and climatological wind at 350 hPa (blue line) and 150 hPa (red line). The dashed black lines show contours of constant angular velocity corresponding to zonal winds of 10, 20, 30, and 40 m s^{-1} at the equator.

shifting the SST field uniformly up and down by ±3 and ±5 K both for the control (T_m = 273 K) and for the T_m = 285 K simulation marking the transition to strong superrotation in the SBM model.

Figure 12b shows that the equatorial upwelling decreases with increasing mean temperature for the control. (Similar results are obtained for T_m = 285 K.) Consistent with the weakening of the Hadley cell drag, superrotation increases with warming in the LSC model (Fig. 12a). In contrast, upper-tropospheric easterlies are found at the equator for the SBM model with T_m = 273 K for both warming and cooling cases, just as in the control. For the T_m = 285 K setting, when an eddy acceleration is present, superrotation strengthens with warming in both models (Fig. 12c).

The lower panels of Fig. 12 show how the subtropical eddy momentum flux divergence and the tropical and extratropical eddy momentum convergence change in these simulations. In SBM with T_m = 273 K, neither the warming nor cooling result in significant eddy equatorial acceleration (Fig. 12f). All other cases have some eddy equatorial acceleration (Figs. 12f,g) and some superrotation, consistent with the claim that some eddy equatorial acceleration is prerequisite for superrotation, regardless of Hadley cell intensity. For T_m = 285 K, the tropical convergence increases slightly with warming for the LSC model, but not for SBM.

The extratropical convergence increases with warming in the T_m = 273 K setting but decreases with warming for T_m = 285 K. Given that the Hadley cell weakens in all cases, only the latter would be compatible with a stress-driven Hadley cell (Walker and Schneider 2006). Consistent with the typical behavior seen in models of this class, the weakening of the Hadley cell with warming is more plausibly thermally controlled, with the increase in subtropical dry stability likely being a key controlling element.

We find that the eastward phase speed of the Kelvin wave increases with warming. While part of this increase may be attributed to the enhanced Doppler shift by the superrotating winds, Fig. 13 suggests that this does not tell the full story. This figure shows scatterplots of the k = 1 Kelvin wave phase speed against the upper-troposphere (150–350 hPa average)

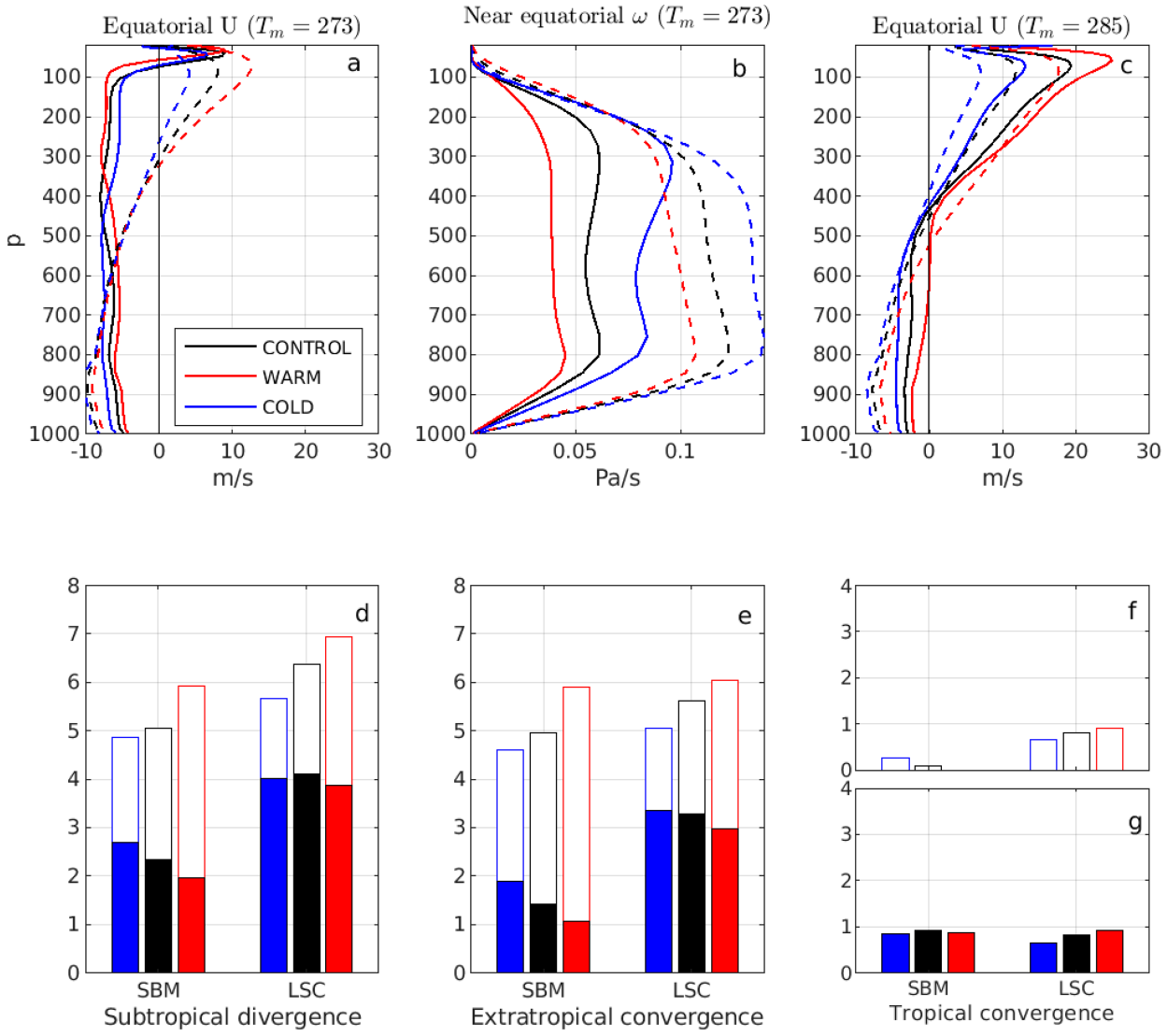

FIG. 12. (a) Equatorial zonal wind for the T_m = 273 K simulation (black) and for a warm and a cold simulation shifting the SST uniformly up or down by 5 K. Solid (dashed) lines are used for SBM (LSC) simulations. (b) As in (a), but for the near-equatorial (5°S–5°N average) upward pressure velocity. (c) As in (a), but for T_m = 285 K. (d) Net subtropical momentum divergence for the same simulations. Unfilled (filled) bars are used for the T_m = 273 K (T_m = 285 K) setting (all bars start from the zero line). (e) As in (d), but for the extratropical momentum convergence (f),(g) As in (d), but for the tropical momentum convergence. For clarity, different panels are used for the T_m = 273 K and T_m = 285 K results in this case.

equatorial zonal wind for the SBM (left) and LSC (right) simulations. (Qualitatively similar results are obtained using the mean tropospheric wind.) As we have shown, superrotation increases both when T_m increases (black asterisks) and when the mean temperature increases (blue/red circles for T_m = 273/285 K). In both cases, this is accompanied by an increase in the Kelvin wave phase speed, consistent with an enhanced Doppler shift by the stronger westerlies. However, the Kelvin phase speed increases with the mean winds much more rapidly in the simulations changing the mean temperature than in the simulations changing T_m, both for SBM and LSC. We do not have a good understanding of how the Kelvin phase speed is determined in this model.

7. Discussion and conclusions

We use an idealized moist GCM to investigate the impact of a weakened and equatorward shifted baroclinic zone on the equatorial upper-troposphere zonal winds. This is achieved by eliminating the SST gradient poleward of a specified latitude in the control Neale and Hoskins (2000) profile, or, equivalently, specifying a temperature T_m that the SST is not allowed to fall below: SST = max[T_m, $SST_{control}$]. Consistent with the dry results of Z22, we find that this modification to the extratropical baroclinicity enhances the superrotation. However, the strength of the superrotation depends on the convective closure for the same SST configuration. We consider two treatments of convection,

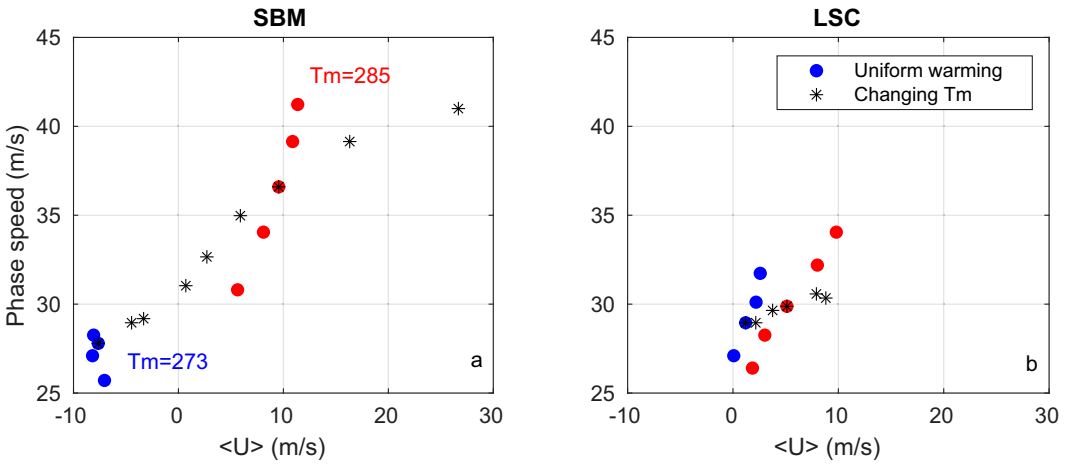

FIG. 13. For the (left) SBM and (right) LSC models, scatterplots of the $k = 1$ Kelvin phase speed against the mean upper-tropospheric wind (150–350-hPa average) in the simulations changing T_m (black asterisks) and in the simulations changing the SSTs uniformly by ±3 and ±5 K (blue/red circles for $T_m = 273/285$ K).

referred to as SBM and LSC, the latter in fact having no parameterized convection. We also examine the sensitivity of superrotation to an increase and decrease in the mean SST; with both convection schemes, the superrotation increases monotonically with increasing mean SST.

As discussed in the introduction, equatorial superrotation is determined by a balance between sources and sinks of angular momentum at the equator. The main momentum source in our simulations is a top heavy meridional eddy momentum convergence dominated by the divergent term $-\overline{u'D'}$, due almost exclusively to zonal wavenumber one. This momentum is redistributed vertically by large scales, for example, by vertically propagating Kelvin waves, and in the LSC model by small scales that are the model's attempt to simulate convective momentum transport. (There is no parameterized convective momentum transport in SBM.) The main drag is provided by the Hadley cell vertical advection, which we assume to be well captured using the mean vertical velocity and zonal wind shear at the equator, even though eddy acceleration events are episodic (section 5).

Thus, we can write above the boundary layer:

$$[\overline{\omega}]\partial_p[\overline{u}] \approx -\overline{u'D'} - \partial_p(\overline{\omega'u'}). \tag{2}$$

Integrating vertically above the boundary layer and neglecting the vertical eddy momentum flux at its top, one then obtains

$$\frac{U_{\max} - U_0}{-\Delta p} \approx \frac{\langle -\overline{u'D'}\rangle}{\langle [\overline{\omega}]\rangle}, \tag{3}$$

where $U_{\max}$ is the maximum tropospheric wind, U_0 is the wind at the top of the boundary layer, Δp is the tropospheric depth above the boundary layer, and $\langle\cdot\rangle$ represents a vertical average. If U_0 and Δp are constant to first order and vertical redistribution by eddies is indeed small, Eq. (3) implies that $U_{\max}$ should vary linearly with $\langle\overline{u'D'}\rangle/\langle[\overline{\omega}]\rangle$. Figure 14 shows that this is reasonably well satisfied in our simulations. A simple linear fit (dashed line) gives $U_0 \approx -8.5$ m s^{-1} and $\Delta p \approx 600$ hPa. Despite the very encouraging agreement for SBM, departure from linearity is observed for the most strongly superrotating LSC simulations. We have not tried to understand this departure quantitatively, but presume that it is due to small-scale mixing of momentum.

Figure 14 helps justify a distinction among the factors that affect superrotation into those that affect the numerator $\langle -\overline{u'D'}\rangle$ and those that affect the denominator $\langle[\overline{\omega}]\rangle$. The effects of perturbations in extratropical eddy fluxes does not appear explicitly in this expression, but must exert their influence

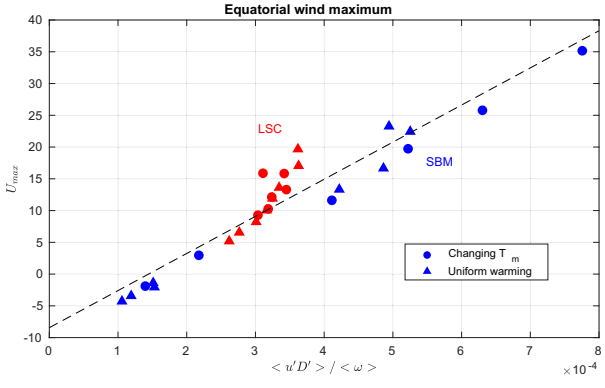

FIG. 14. Scatterplot of the tropospheric equatorial wind maximum against $\langle\overline{u'D'}\rangle/\langle[\overline{\omega}]\rangle$, with $\overline{u'D'}$ averaged over the upper troposphere (100–500 hPa) and $[\overline{\omega}]$ averaged over the full troposphere (100–1000 hPa). All variables are meridional averages within 10° of the equator. We use blue (red) markers for SBM (LSC). The filled circles show results for the simulations varying T_m and the filled triangles for the simulations adding a uniform SST warming/cooling. The dashed line shows the best linear fit (correlation coefficient 0.95).

on either the equatorial acceleration due to ageostrophic eddies or the strength of the equatorial upwelling in the Hadley cell.

Given the balance in Eq. (3), superrotation requires a positive $\langle -\overline{u'D'} \rangle$. The LSC model produces this in all cases examined. In SBM, the eddy forcing is negligible in the control but increases when T_m is large. Our starting point for analyzing this eddy forcing is Kelvin–Rossby instability, or, more generally, two-way interaction between the equatorial Kelvin wave and subtropical Rossby waves. Consistent with this picture, Fig. 8 shows that a significant part of the equatorial acceleration $\langle -\overline{u'D'} \rangle$ that develops in the SBM model with increasing T_m is associated with the rotational zonal wind induced by vorticity anomalies outside of the deep tropics. Examination of the internal variability of the equilibrated model in the superrotating regime shows that instances of large equatorial eddy forcing tend to be preceded by enhanced meridional shear of the zonal flow in the upper troposphere a few days earlier. This is reminiscent of the recent study of Barpanda et al. (2023) that provides evidence that subtropical Rossby waves enhance equatorial convection when the subtropical jet is strong.

In the dry model study in Z22, a picture was proposed of the interaction between the equatorial Kelvin waves and Rossby waves riding on the subtropical jet (in analogy with the baroclinic interaction between upper- and lower-tropospheric edge waves). In this picture, the speed of the subtropical jet is an important factor in allowing the synchronization of wave phase speeds, and extratropical eddy heat and momentum fluxes can alter the strength of this interaction by altering the subtropical jet. In the present moist model, however, we do not see a consistent difference between the subtropical jet strengths in simulations that superrotate and those that do not. So we have no convincing theory for how the altered extratropical eddy fluxes directly affected by increasing T_m control the Kelvin–Rossby interaction.

Such a theory would hopefully also explain the differences in the eddy equatorial acceleration between the LSC and SBM models. These differences could be due to differences in the pre-existing convectively generated Kelvin wave. But the Kelvin wave phase speed is similar in the control simulations in the two models. Differences in phase speed only develop when the stronger superrotation arises in SBM. And examination of composites shows no features that would explain the larger eddy acceleration in the control LSC.

We are closer to a qualitative understanding of how the strength of the Hadley cell and the extratropical eddies that modify that strength affect superrotation through the denominator in Eq. (3). We find that the Hadley cell weakens in both models when T_m increases, but more strongly for SBM. This weakening is clearly related to weakening of the poleward eddy energy and angular momentum transports out of the subtropics. The relative importance of eddy energy and momentum transports is dependent on whether the Hadley cell is predominantly in a low-Rossby number momentum controlled state or is more nonlinear and thermally controlled (or, more realistically, with thermal control in the deep tropics transitioning to momentum control nearer to the subtropical edge). We do not attempt here to quantify these different pathways.

The resulting effect on superrotation is large. If we start from the SBM control and increase T_m, the superrotation must first result from the numerator in Eq. (3), but with increasing T_m, the superrotation enhancement is quickly dominated by the reduction in Hadley drag. For instance, for the SBM simulation with $T_m = 285$ K, superrotation is 70% larger than that predicted by Eq. (3) with the same eddy forcing when the equatorial upwelling is unchanged from control.

Once substantial superrotation is generated, a positive feedback develops due to the disappearance of critical latitudes in the tropics where baroclinically produced Rossby waves break, as seen in the latitude-phase speed spectra of the eddy momentum flux in Fig. 11. As implied by the good fit in Fig. 14, we evidently can think of this loss of wave drag as affecting the superrotation through the consequent reduction in Hadley cell strength. The differences between the superrotation strengths in LSC and SBM become enhanced when this feedback develops in one model and not the other. The implication is that it is the stronger Hadley cell in LSC that ultimately prevents this feedback from emerging in LSC.

Another potential feedback affecting the Hadley cell strength is that due to axisymmetric dynamics as described in Shell and Held (2004): the warmer equatorial troposphere associated with superrotation through the thermal wind constraint increases the meridional gradient across the tropics, a gradient that is maintained against radiative forcing by a weaker Hadley cell, strengthening the superrotation further. But additional analysis will be needed to determine if this mechanism plays a significant quantitative role in the current model.

The Hadley cell weakens in both models with uniform warming. This response is common in aquaplanet models with various levels of idealization (Medeiros et al. 2015). Because there is no equatorial eddy acceleration in the SBM control, this reduction in Hadley strength does not create superrotation in that case, consistent with Eq. (3). In the other cases, with positive eddy acceleration, the superrotation increases. Although there is some increase in the eddy acceleration with warming in the LSC simulations, the reduction in Hadley cell strength is the dominant factor enhancing superrotation in this case as well.

The role of the Hadley cell drag in limiting superrotation in our simulations is consistent with the analysis of Pinto and Mitchell (2014) on the sensitivity of an idealized dry dynamical core to changes in orbital parameters. With the same thermal Rossby number, these authors found stronger superrotation when the planet radius is reduced than when the rotation rate is reduced. They noted that this occurs because with the same thermal damping rate, the Hadley cell weakens when reducing the planet radius but strengthens when decreasing the rotation rate. This is in contrast to the speculation of Z22 that a stronger Hadley cell might promote superrotation by accelerating the subtropical jet, which does not happen in our simulations. It is plausible that the sensitivity of superrotation to Hadley cell strength may be regime dependent and sensitive to the constraints determining the speed of the subtropical jet.

The bulk of our simulations involve a particular modification to the prescribed SSTs in order to facilitate superrotation—we have reduced extratropical SST gradients while holding tropical gradients fixed. Thakur et al. (2024) have recently presented results with an aquaplanet version of CAM6 in which the tropical and extratropical SST gradients are reduced simultaneously. While they do not focus on superrotation, their results indicate that superrotation does develop with this reduction in gradient. We have followed up to perform the same SST modification in our more idealized model and find results that are distinct from those described here (and distinct from those presented in Thakur et al.) Further study will be needed to determine how these differences can inform our understanding of the transition to superrotation.

The different sensitivity of superrotation in the SBM and LSC models suggests that the convective closure may play an important role for the susceptibility of a model to superrotate more generally. While it seems that Hadley cell strength is a metric through which one can understand much of this sensitivity in our simulations, this may not be the case more generally. An unrealistic aspect of our simulations is its convectively coupled wave spectrum: the Kelvin wave is relatively fast and there is no significant MJO variability. Sensitivity to convection scheme could be determined in part by this convectively coupled equatorial wave spectrum.

Cumulus momentum transport (CMT) may be another aspect of convective closure potentially important for superrotation. The SBM convection scheme used in this paper has no CMT, while the LSC model, with no parameterized convection, cannot be expected to provide very meaningful CMT on its resolved scales. CMT is likely to be sensitive to convective organization, and the type of organization in the strong vertical shears in a superrotating state may be distinct from those familiar in the present climate. Our results on sensitivity to treatment of moist convection only touch the surface of potential sensitivities relevant for past and future warm climates on Earth.

Despite these convective sensitivities, this study supports the claim that extratropical baroclinically generated eddy fluxes play a critical role in suppressing superrotation on Earth. As in the dry model of Z22, the subtropical drag due to these eddies can be reduced by moving the baroclinic zone equatorward, suppressing anticyclonic wave breaking. A combination of weakened Hadley cell strength due to warming, other forcing factors encouraging merger of the extratropical and subtropical jets, and feedback due to the disappearance of low-latitude Rossby wave critical layers could favor strong superrotation in warm climates.

Acknowledgments. We are grateful to Jonathan Mitchell, Neil Lewis and an anonymous reviewer for their insightful and constructive comments. PZG is funded by Grant PID2022-136316NB-I00 by MCIN/AEI/10.13039/501100011033. Support from NSF Grant AGS 2246700 is gratefully acknowledged.

Data availability statement. The simulations described in this paper were performed using the Isca model, publicly available at https://execlim.github.io/IscaWebsite/. A sample runscript is included in the supplemental material to facilitate reproducibility of our results.

REFERENCES

Balasubramanian, G., and S. T. Garner, 1997: The role of momentum fluxes in shaping the life cycle of a baroclinic wave. *J. Atmos. Sci.*, **54**, 510–533, https://doi.org/10.1175/1520-0469(1997)054<0510:TROMFI>2.0.CO;2.

Barpanda, P., S. N. Tulich, J. Dias, and G. N. Kiladis, 2023: The role of subtropical Rossby waves in amplifying the divergent circulation of the Madden–Julian oscillation. *J. Atmos. Sci.*, **80**, 2377–2398, https://doi.org/10.1175/JAS-D-22-0259.1.

Blackburn, M., and Coauthors, 2013: The Aqua-Planet Experiment (APE): Control SST simulation. *J. Meteor. Soc. Japan*, **91A**, 17–56, https://doi.org/10.2151/jmsj.2013-A02.

Caballero, R., and M. Huber, 2010: Spontaneous transition to superrotation in warm climates simulated by CAM3. *Geophys. Res. Lett.*, **37**, L11701, https://doi.org/10.1029/2010GL043468.

——, and H. Carlson, 2018: Surface superrotation. *J. Atmos. Sci.*, **75**, 3671–3689, https://doi.org/10.1175/JAS-D-18-0076.1.

Davis, C. A., 1992: Piecewise potential vorticity inversion. *J. Atmos. Sci.*, **49**, 1397–1411, https://doi.org/10.1175/1520-0469(1992)049<1397:PPVI>2.0.CO;2.

Dima, I. M., J. M. Wallace, and I. Kraucunas, 2005: Tropical zonal momentum balance in the NCEP reanalyses. *J. Atmos. Sci.*, **62**, 2499–2513, https://doi.org/10.1175/JAS3486.1.

Fang, M., and K. K. Tung, 1996: A simple model of nonlinear Hadley circulation with an ITCZ: Analytic and numerical solutions. *J. Atmos. Sci.*, **53**, 1241–1261, https://doi.org/10.1175/1520-0469(1996)053<1241:ASMONH>2.0.CO;2.

Frierson, D. M. W., 2007a: The dynamics of idealized convection schemes and their effect on the zonally averaged tropical circulation. *J. Atmos. Sci.*, **64**, 1959–1976, https://doi.org/10.1175/JAS3935.1.

——, 2007b: Convectively coupled Kelvin waves in an idealized moist general circulation model. *J. Atmos. Sci.*, **64**, 2076–2090, https://doi.org/10.1175/JAS3945.1.

——, I. M. Held, and P. Zurita-Gotor, 2006: A gray-radiation aquaplanet moist GCM. Part I: Static stability and eddy scale. *J. Atmos. Sci.*, **63**, 2548–2566, https://doi.org/10.1175/JAS3753.1.

Held, I. M., and M. J. Suarez, 1994: A proposal for the intercomparison of the dynamical cores of atmospheric general circulation models. *Bull. Amer. Meteor. Soc.*, **75**, 1825–1830, https://doi.org/10.1175/1520-0477(1994)075<1825:APFTIO>2.0.CO;2.

Hide, R., 1969: Dynamics of the atmospheres of the major planets with an appendix on the viscous boundary layer at the rigid bounding surface of an electrically-conducting rotating fluid in the presence of a magnetic field. *J. Atmos. Sci.*, **26**, 841–853, https://doi.org/10.1175/1520-0469(1969)026<0841:DOTAOT>2.0.CO;2.

Iga, S.-i., and Y. Matsuda, 2005: Shear instability in a shallow water model with implications for the Venus atmosphere. *J. Atmos. Sci.*, **62**, 2514–2527, https://doi.org/10.1175/JAS3484.1.

Imamura, T., J. Mitchell, S. Lebonnois, Y. Kaspi, A. P. Showman, and O. Korablev, 2020: Superrotation in planetary atmospheres. *Space Sci. Rev.*, **216**, 87, https://doi.org/10.1007/s11214-020-00703-9.

Jucker, M., and E. P. Gerber, 2017: Untangling the annual cycle of the tropical tropopause layer with an idealized moist model. *J. Climate*, **30**, 7339–7358, https://doi.org/10.1175/JCLI-D-17-0127.1.

Lan, J., and Coauthors, 2023: Weak equatorial superrotation during the past 250 million years. *J. Atmos. Sci.*, **80**, 1003–1023, https://doi.org/10.1175/JAS-D-22-0072.1.

Laraia, A. L., and T. Schneider, 2015: Superrotation in terrestrial atmospheres. *J. Atmos. Sci.*, **72**, 4281–4296, https://doi.org/10.1175/JAS-D-15-0030.1.

Lee, S., 1999: Why are the climatological zonal winds easterly in the equatorialupper troposphere? *J. Atmos. Sci.*, **56**, 1353–1363, https://doi.org/10.1175/1520-0469(1999)056<1353:WATCZW>2.0.CO;2.

——, and H.-k. Kim, 2003: The dynamical relationship between subtropical and eddy-driven jets. *J. Atmos. Sci.*, **60**, 1490–1503, https://doi.org/10.1175/1520-0469(2003)060<1490:TDRBSA>2.0.CO;2.

Lewis, N. T., N. A. Lombardo, P. L. Read, and J. M. Lora, 2023: Equatorial waves and superrotation in the stratosphere of a Titan general circulation model. *Planet. Sci. J.*, **4**, 149, https://doi.org/10.3847/PSJ/ace76f.

Lewis, S. R., and P. L. Read, 2003: Equatorial jets in the dusty Martian atmosphere. *J. Geophys. Res.*, **108**, 5034, https://doi.org/10.1029/2002JE001933.

Medeiros, B., B. Stevens, and S. Bony, 2015: Using aquaplanets to understand the robust responses of comprehensive climate models to forcing. *Climate Dyn.*, **44**, 1957–1977, https://doi.org/10.1007/s00382-014-2138-0.

Mitchell, J. L., and G. K. Vallis, 2010: The transition to superrotation in terrestrial atmospheres. *J. Geophys. Res.*, **115**, E12008, https://doi.org/10.1029/2010JE003587.

Mlawer, E. J., S. J. Taubman, P. D. Brown, M. J. Iacono, and S. A. Clough, 1997: Radiative transfer for inhomogeneous atmospheres: RRTM, a validated correlated-k model for the longwave. *J. Geophys. Res.*, **102**, 16 663–16 682, https://doi.org/10.1029/97JD00237.

Neale, R. B., and B. J. Hoskins, 2000: A standard test for AGCMs including their physical parametrizations: I: The proposal. *Atmos. Sci. Lett.*, **1**, 101–107, https://doi.org/10.1006/asle.2000.0022.

Neelin, J. D., and I. M. Held, 1987: Modeling tropical convergence based on the moist static energy budget. *Mon. Wea. Rev.*, **115**, 3–12, https://doi.org/10.1175/1520-0493(1987)115<0003:MTCBOT>2.0.CO;2.

Newman, C. E., C. Lee, Y. Lian, M. I. Richardson, and A. D. Toigo, 2011: Stratospheric superrotation in the TitanWRF model. *Icarus*, **213**, 636–654, https://doi.org/10.1016/j.icarus.2011.03.025.

O'Gorman, P. A., and T. Schneider, 2008: The hydrological cycle over a wide range of climates simulated with an idealized GCM. *J. Climate*, **21**, 3815–3832, https://doi.org/10.1175/2007JCLI2065.1.

Pinto, J. R. D., and J. L. Mitchell, 2014: Atmospheric superrotation in an idealized GCM: Parameter dependence of the eddy response. *Icarus*, **238**, 93–109, https://doi.org/10.1016/j.icarus.2014.04.036.

Potter, S. F., G. K. Vallis, and J. L. Michell, 2014: Spontaneous superrotation and the role of Kelvin waves in an idealized dry GCM. *J. Atmos. Sci.*, **71**, 596–614, https://doi.org/10.1175/JAS-D-13-0150.1.

Sakai, S., 1989: Rossby-Kelvin instability: A new type of ageostrophic instability caused by a resonance between Rossby waves and gravity waves. *J. Fluid Mech.*, **202**, 149–176, https://doi.org/10.1017/S0022112089001138.

Saravanan, R., 1993: Equatorial superrotation and maintenance of the general circulation in two-level models. *J. Atmos. Sci.*, **50**, 1211–1227, https://doi.org/10.1175/1520-0469(1993)050<1211:ESAMOT>2.0.CO;2.

Shell, K. M., and I. M. Held, 2004: Abrupt transition to strong superrotation in an axisymmetric model of the upper troposphere. *J. Atmos. Sci.*, **61**, 2928–2935, https://doi.org/10.1175/JAS-3312.1.

Singh, M. S., and Z. Kuang, 2016: Exploring the role of eddy momentum fluxes in determining the characteristics of the equinoctial Hadley circulation: Fixed-SST simulations. *J. Atmos. Sci.*, **73**, 2427–2444, https://doi.org/10.1175/JAS-D-15-0212.1.

Suarez, M. J., and D. G. Duffy, 1992: Terrestrial superrotation: A bifurcation of the general circulation. *J. Atmos. Sci.*, **49**, 1541–1554, https://doi.org/10.1175/1520-0469(1992)049<1541:TSABOT>2.0.CO;2.

Suhas, D. L., J. Sukhatme, and J. M. Monteiro, 2017: Tropical vorticity forcing and superrotation in the spherical shallow-water equations. *Quart. J. Roy. Meteor. Soc.*, **143**, 957–965, https://doi.org/10.1002/qj.2979.

Takagi, M., H. Ando, N. Sugimoto, and Y. Matsuda, 2022: A GCM study on the 4-day and 5-day waves in the Venus atmosphere. *J. Geophys. Res. Planets*, **127**, e2021JE007164, https://doi.org/10.1029/2021JE007164.

Thakur, A. B. S., J. Sukhatme, and N. Harnik, 2024: Investigating the role of tropical and extratropical waves in the Hadley circulation via present-day earth-like to globally uniform sea-surface temperature forcing. *Quart. J. Roy. Meteor. Soc.*, **150**, 3578–3600, https://doi.org/10.1002/qj.4784.

Vallis, G. K., and Coauthors, 2018: Isca, v1.0: A framework for the global modelling of the atmospheres of Earth and other planets at varying levels of complexity. *Geosci. Model Dev.*, **11**, 843–859, https://doi.org/10.5194/gmd-11-843-2018.

Walker, C. C., and T. Schneider, 2006: Eddy influences on Hadley circulations: Simulations with an idealized GCM. *J. Atmos. Sci.*, **63**, 3333–3350, https://doi.org/10.1175/JAS3821.1.

Wang, P., and J. L. Mitchell, 2014: Planetary ageostrophic instability leads to superrotation. *Geophys. Res. Lett.*, **41**, 4118–4126, https://doi.org/10.1002/2014GL060345.

Webster, P. J., and J. R. Holton, 1982: Cross-equatorial response to middle-latitude forcing in a zonally varying basic state. *J. Atmos. Sci.*, **39**, 722–733, https://doi.org/10.1175/1520-0469(1982)039<0722:CERTML>2.0.CO;2.

Williams, G. P., 2003: Barotropic instability and equatorial superrotation. *J. Atmos. Sci.*, **60**, 2136–2152, https://doi.org/10.1175/1520-0469(2003)060<2136:BIAES>2.0.CO;2.

Yamamoto, M., T. Hirose, K. Ikeda, M. Takahashi, and M. Satoh, 2023: Short-period planetary-scale waves in a Venus general circulation model: Rotational and divergent component structures and energy conversions. *Icarus*, **392**, 115392, https://doi.org/10.1016/j.icarus.2022.115392.

Zhang, P., and N. J. Lutsko, 2022: Seasonal superrotation in Earth's troposphere. *J. Atmos. Sci.*, **79**, 3297–3314, https://doi.org/10.1175/JAS-D-22-0066.1.

Zurita-Gotor, P., 2019: The role of the divergent circulation for large-scale eddy momentum transport in the tropics. Part I: Observations. *J. Atmos. Sci.*, **76**, 1125–1144, https://doi.org/10.1175/JAS-D-18-0297.1.

——, and I. M. Held, 2018: The finite-amplitude evolution of mixed Kelvin–Rossby wave instability and equatorial superrotation in a shallow-water model and an idealized GCM. *J. Atmos. Sci.*, **75**, 2299–2316, https://doi.org/10.1175/JAS-D-17-0386.1.

——, Á. Anaya-Benlliure, and I. M. Held, 2022: The sensitivity of superrotation to the latitude of baroclinic forcing in a terrestrial dry dynamical core. *J. Atmos. Sci.*, **79**, 1311–1323, https://doi.org/10.1175/JAS-D-21-0269.1.

——, I. M. Held, T. M. Merlis, C.-Y. Chang, S. A. Hill, and C. G. MacDonald, 2023: Non-uniqueness in ITCZ latitude due to radiation-circulation coupling in an idealized GCM. *J. Adv. Model. Earth Syst.*, **15**, e2023MS003736, https://doi.org/10.1029/2023MS003736.